Biological and Biomedical Journal

Journal homepage: https://bbj.journals.ekb.eg

Histological study of subcutaneous injections of nanofat versus hyaluronic acid on thin skin of female aged albino rats

Hagar O. Megahed, Noha R. Elswaidy, Naglaa I. Sarhan, Shereen Sh. Elabd*

Histology and Cell Biology Department, Faculty of Medicine, Tanta University, Egypt

ARTICLE INFO

Received: 3/12/2024
Accepted: 30/12/2024

* **Corresponding author:**
Shereen Sh. Elabd, MD
E-mail:
shereen.elabd@med.tanta.edu.eg
Mobile: (+2)01006269505

P-ISSN: 2974-4334
E-ISSN: 2974-4324
DOI:
10.21608/bbj.2024.341336.1061

ABSTRACT

Skin ageing is an inevitable process characterized by loss of elasticity and decreased dermal volume. Nanofat injection is a new technique used for long-lasting skin rejuvenation, while hyaluronic acid (HA) is widely used to improve skin rejuvenation temporarily. This work aimed to compare the effect of nanofat versus hyaluronic acid (HA) subcutaneous injections on the aged thin skin of female rats. Four equal groups of 40 female rats were included in this study. Group I (GpI) was the control adult, while GpII was the control aged one. GpIII aged rats received a single subcutaneous (SC) injection of 0.1 ml of cross-linked HA, while Gp IV-aged rats received a single SC injection of 0.1 ml of nanofat. Light microscopic examination was done following staining with H&E, Masson trichrome, and anti-vascular endothelial growth factor (VEGF) immunostaining, in addition to electron microscopic study. The light and electron microscopic examination of GpIII and GpIV revealed structural rejuvenation of their aged skin. In the papillary dermis, collagen fibers were fine, interlocking small bundles. In the reticular dermis, they appeared as thick, closely packed bundles, with elastic fibers and active fibroblasts in between. Morphometric analysis displayed a significant increase in the mean total thickness of the dermis, mean area percentage of Masson trichrome-stained collagen fibers, and mean number of positive VEGF blood vessels of both GpIII and GpIV compared to group II. In conclusion, nanofat and HA subcutaneous injections improved skin ageing signs; however, nanofat injection is particularly predominant in neovascularisation and collagen formation.

Key words: Aged skin, Electron microscope, Hyaluronic acid, Nanofat, VEGF.

1. Introduction

Skin ageing is a natural and time-dependent process that occurs due to a complex interaction between intrinsic and extrinsic factors (Wong and Chew, 2021; Liang et al., 2023). Intrinsic skin ageing factors includes genetic and hormonal changes. The theory of intrinsic ageing is broadly divided into telomere shortening, decrease in DNA repair, and oxidative stress (Kerns and Chien, 2019). Extrinsic ageing includes preventable environmental factors such as ultraviolet radiation, nutrition, alcohol consumption, and tobacco use (Krutmann et al., 2021). Cellular senescence is a multifaceted phenomenon marked by irreversible cell cycle arrest, apoptosis resistance, and secretion of factors that promote tissue deterioration and inflammation (Gruber et al., 2020; Pilkington et al., 2021). Senescent keratinocytes release elevated amounts of inflammatory cytokines, immunological modulators, and matrix metalloproteinases (MMP), resulting in detrimental effects and inflammation (Birch and Gil, 2020). The proteolytic enzymes MMP and

collagenase are responsible for the degradation of collagen fibers and matrix components. The wrinkles, loss of elasticity, and reduced dermal volume associated with skin ageing are caused by decreased collagen production and altered elastin network structure (Ho and Dreesen, 2021; Lynch et al., 2022). The decline of collagen fibers in aged skin is associated with a disparity between collagen synthesis and breakdown by MMP-1. Inhibition of MMP and stimulation of collagen production in dermal fibroblasts are effective methods for mitigating the manifestations of skin ageing (Shin et al., 2019). Dermal fillers have gained popularity in recent years for the goal of long-lasting skin rejuvenation. They are simple, quick-acting, minimally invasive, and quick-recovery cosmetic interventions used to contour, lift, and enhance volume of skin (Guo et al., 2023).

Hyaluronic acid (HA) is a non-sulphated glycosaminoglycan that serves as a natural constituent of the extracellular matrix. The injectable cross-linked HA is a gold standard, and the commonest type used nowadays as a temporary dermal filler for its safety and efficacy in reducing wrinkles and restoring volume loss (Allen and Dodou, 2024). Nanofat is an ultra-purified adipose tissue-derived product obtained by mechanical emulsification and filtration of the lipo-aspirates (Tonnard et al., 2013). Nanofat lacks mature adipocytes but is rich in stromal vascular fractions (SVF) and growth factors such as CD34-positive adipose-derived mesenchymal stem cells (ADSCs), vascular endothelial growth factor (VEGF), platelet-derived growth factor (PDGF), transforming growth factor-beta (TGF-β), basic fibroblast growth factor (bFGF), and granulocyte-macrophage colony-stimulating factor (GM-CSF). The SVF includes adipocyte precursor cells, fibroblasts, vascular smooth muscle cells, endothelial cells, resident monocytes (macrophages), lymphocytes, and ADSCs (Sharma et al., 2021). Nowadays, nanofat has been used for its anti-ageing effect as a long-lasting soft tissue filler because it can improve skin quality and restore the volume through the effect of the mesenchymal stromal cells (Ding et al., 2022; Mamizadeh et al., 2024). Based on the previous data, this study is designed to analyse the effect of subcutaneous injections of nanofat versus hyaluronic acid dermal filler on the aged thin skin of female albino rats.

2. Materials and methods

This work was conducted on forty female albino rats consisting of ten adult rats (aged 6–8 months and weighing 150–200 g) and thirty aged rats (aged 12 months and weighing 250–300 g). All the rats were housed in clean, well-ventilated cages, maintaining a temperature range of 20–25 °C, relative humidity, and a 12-hour light/dark cycle. They were also provided with the same commercial laboratory diet and water. The Research Ethical Committee of Tanta University's Faculty of Medicine approved the study, with the approval code (36206/12/22).

The experimental design

The animals were divided into: Group I (GpI, control-adult rats): the adult rats were kept without any treatment. Then the aged animals were divided randomly and equally into three groups: GpII (control-aged group): the aged rats were subdivided into two equal subgroups: Subgroup IIa was kept without treatment till the end of the experiment. The fatty tissue used in the preparation of nanofat was harvested from this subgroup (negative control). Subgroup IIb received a single subcutaneous (SC.) injection of 0.1 ml of normal saline at the right flank region (sham group) and sacrificed after 30 days.

Group III (Hyaluronic acid-treated group): the aged rats received a single SC. injection of 0.1 ml of cross-linked hyaluronic acid at the right flank, then were sacrificed and dissected after 30 days (Jung-Bo et al., 2015; Aziz et al., 2019). GpIV (Nanofat-treated group): the rats received a single SC. injection of 0.1 ml of nanofat at the right flank region and were sacrificed and dissected after 30 days (Simonacci et al., 2019).

Chemicals

The cross-linked hyaluronic acid was obtained under the brand name “BELOTERO BALANCE LIDOCAINE” from the Merz Aesthetics Company, Germany. It was purchased as a prepared glass syringe that contains 1 ml of cross-linked hyaluronic acid with lidocaine for relieving the pain.

Preparation of nanofat injection

The macrofat was extracted from the adipose tissue collected from subgroup IIa following the

standardized protocol established by Tonnard et al. (2013). The adipose tissue was eliminated from the inguinal and perirenal subcutaneous regions (Plate I-a), cut up producing uniform fat fragments (1 x 1 x 1 mm), resulting in microfat, and rinsed in a 0.9% NaCl solution under strict aseptic conditions (Plate I-b) (Weinzierl et al., 2022). Mechanical emulsification was performed by shifting the microfat between two 10-cc syringes linked by a 3-way adapter (Plate I-c). After 20–30 passes, the fat transforms into an emulsion. This process was repeated until the nanofat liquefied and attained a whitish appearance.

The emulsified fatty liquid was filtered through a sterile nylon cloth to eliminate connective tissue remains that could obstruct the fine needles. The effluent obtained is referred to as "Nanofat" (Plate I-d). The nanofat was injected subcutaneously once at a dose of 0.1 ml using a 27-gauge needle in the right flank region (Plate I-e). At the end of the experiment, the animals were euthanized via intraperitoneal injection of sodium thiopental (30 mg/kg) (Kushawaha et al., 2011). The skin samples were dissected from the right flank region and processed for histological preparation. The sacrificed animals were packaged in accordance with safety procedures and infection control measures and dispatched to the hospital hazards.

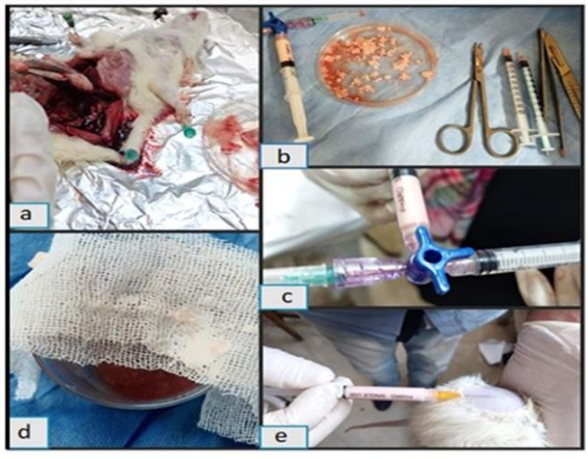

Plate. I. The photo illustrates the steps involved in the preparation of nanofat, including extracting the fatty tissue (a), mincing the harvested fatty tissue into tiny 1 mm3 cubes (b), mechanically emulsifying the microfat using a 3-way adapter (c), filtering the nanofat through a sterile nylon cloth (d), and finally injecting the nanofat subcutaneously in the right flank region (e).

Histological examination

The skin specimens were fixed in 10% formal saline solution, subsequently washed, dehydrated with ascending grades of alcohol, cleared in two changes of xylene, impregnated with soft paraffin at 60° C for 2 hours, and finally embedded in hard paraffin (Bancroft and Layton, 2019). Lastly, sections of 5 µm thickness had been cut for the following studies: haematoxylin and eosin (H&E), Masson's trichrome and immunohistochemical stain.

Immunohistochemical study

Anti-VEGF serves as a marker for angiogenesis, indicating the development of new blood vessels. The deparaffinized sections were rehydrated, treated in 3% hydrogen peroxide for 10 - 15 minutes, and microwaved in preheated citrate buffer solution (pH 6) for 10–20 minutes. After cooling and washing, the sections were incubated overnight at 4°C in a humid chamber with the primary antibody VEGF (RB-9031-P-A, polyclonal, Thermo Fisher Scientific, Massachusetts, USA) at a 1:100 dilution and subsequently washed three times with phosphate-buffered saline (PBS). The sections were subsequently treated with biotinylated goat anti-rabbit secondary antibodies for one hour at room temperature. Streptavidin-biotin-horseradish peroxidase was added for an additional hour at room temperature and rinsed three times. The immunoreaction was visualized using 3,3'-diaminobenzidine (DAB) for a duration of 10 minutes. The slides were subsequently cleaned, counterstained with Mayer's haematoxylin, dehydrated, and lastly mounted. Cellular localization of VEGF is cytoplasmic, cell surface, and in the extracellular matrix. Positive control for VEGF was angiosarcoma. Negative control was run automatically by omitting the primary antibody (Nguyen, 2022).

Preparation of ultrathin sections for transmission electron microscopic

Skin fragments (1 mm^3) were fixed in 2.5% phosphate-buffered glutaraldehyde (pH 7.4) for 24 hours. After being fixed in 1% phosphate buffer osmium tetroxide for 30 minutes, the samples were rinsed in phosphate buffer and dried out by adding more and more alcohol at 4°C (Kuo, 2016). Ultrathin sections (60 nm

thick) were cut, mounted on copper grids, and stained three times with lead citrate and uranyl acetate. Stained sections were observed using a JEOL-JEM-100 SX electron microscope at the Electron Microscopic Unit of the Histology and Cell Biology Department, Faculty of Medicine, Tanta University.

Morphometric study

The software "Image J, (1.48v)" was used for image analysis obtained from the National Institute of Health, Bethesda, Maryland, USA for morphometric study of the specimens. Ten different, non-overlapping, randomly selected fields from each slide from each rat of each group were microscopically examined.

The following parameters were quantified:

The mean total thickness of the dermis in H&E-stained sections (at a magnification power of 200x) was measured from basal lamina to adipose tissue. The mean area percentage of collagen fibers in Masson trichrome stained sections (at a magnification power of 400x). The mean number of blood vessels positive for VEGF in immunostained sections (at a magnification power of 400x).

Statistical analysis

The results were analyzed using one-way analysis of variance (ANOVA), then the Tukey's test was used as a post-comparison test using Microsoft office Excel 2010 for Windows (Microsoft Corporation, Redmond, Washington, USA). All values were expressed as mean $\pm$ standard deviation (SD) and the changes were considered significant if the probability (p) values were less than 0.001 and were considered non-significant if the P values were more than 0.001 (Dawson-Saunders and Trapp, 2001).

3. Results

Hematoxylin and eosin staining

Examination of thin skin sections of the control adult group (GpI) was similar to the normal structure of the epidermis and dermis. The epidermis consisted of stratified squamous keratinized epithelium organized into the known four layers; stratum basale, spinosum, granulosum, and the outermost stratum corneum that was consisted of parallel, acidophilic keratin lamellae. The dermis comprised two layers: the superficial papillary layer, which consists of loose areolar connective tissue containing fine interlaced collagen fibers and blood capillaries; and the deep reticular layer, composed of tightly packed, coarse collagen bundles, and numerous hair follicles associated with sebaceous glands. The epidermis and dermis were interconnected by rete ridges and dermal papillae establishing the clearly defined epidermal-dermal junction. The subcutaneous tissue consisted of an outward layer of adipose tissue, a middle layer of striated muscle, and an inner layer of loose connective tissue (Fig. 1). The findings of both subgroups IIa and IIb (aged control GpII) were consistent, demonstrating an apparent decrease in the epidermal thickness in some regions, focal areas of abnormal keratinocytes with deep homogeneous acidophilic cytoplasm, and darkly stained flattened nuclei. The epidermal-dermal junction was flattened and showed effacement of the rete ridges with focal separation of the epidermis from the underlying dermis. The superficial dermis exhibited irregular collagen fibre configuration, featuring disorganized, tangled, fragmented, and widely spaced fibers; moreover, the whole dermis revealed focal variable-sized empty spaces. The subcutaneous tissue appeared relatively thin with thinning of the adipose tissue layer as well as the striated muscle layer (Fig. 2).

Examination of HA-injected group (GpIII) demonstrated that the epidermis and dermis closely resembled the picture seen in the control adult rats. The epidermis consisted of the four typical layers featuring a distinct epidermal-dermal junction. The whole dermis showed absence of the empty spaces and exhibited well-organized, densely packed collagen fibers with dispersed fibroblasts. At the injection site, the HA filler significantly augmented the thickness of the subcutaneous tissue. The basophilic HA filler was uniformly distributed and well-integrated with the adjacent connective tissue with absence of inflammatory cells. Multiple integrated collagen fibers of varying thickness were observed extending like spearheads from the periphery of the filling material, alongside islands of connective tissue within its substance

(Fig. 3). The examination of the epidermis and dermis of nanofat-injected group (GpIV) displayed a morphological resemblance to the control adult group featuring a prominent epidermal-dermal junction, and small epidermal ridges in some regions. The dermis exhibited an increase in both the amount and density of collagen fibers relative to group II. Increased numbers of blood vessels were noted in the dermis and surrounding the area of nanofat injection along with the superficial layer of adipose tissue in comparison to GpII and GpIII. Regarding the subcutaneous area of nanofat injection, there was an obvious increase in the thickness.

The region beneath the muscle was occupied by adipose connective tissue below the areolar connective tissue, expressing many unilocular adipocytes compartmentalised by connective tissue islands. The islands showed increased cellularity, vascularity, inflammatory cells, and wavy acidophilic collagen fibers in conjunction with areas containing eccrine sweat glands. The secretory part of the eccrine sweat gland displayed three cell types: dark, clear, and flattened myoepithelial cells (Fig.4). Morphometric analysis of the mean dermal thickness of aged control GpII (769.549±69.010) revealed a significant decrease compared to adult GpI (955.452 ±60.985). There was a significant increase of GpIII (885.009±66.09) and GpIV (893.905±64.080) in comparison with GpII (769.549±69.010). A non-significant change was detected in the mean total dermal thickness of GpIII and GpIV as compared to GpI (Table 1) (Histogram 1).

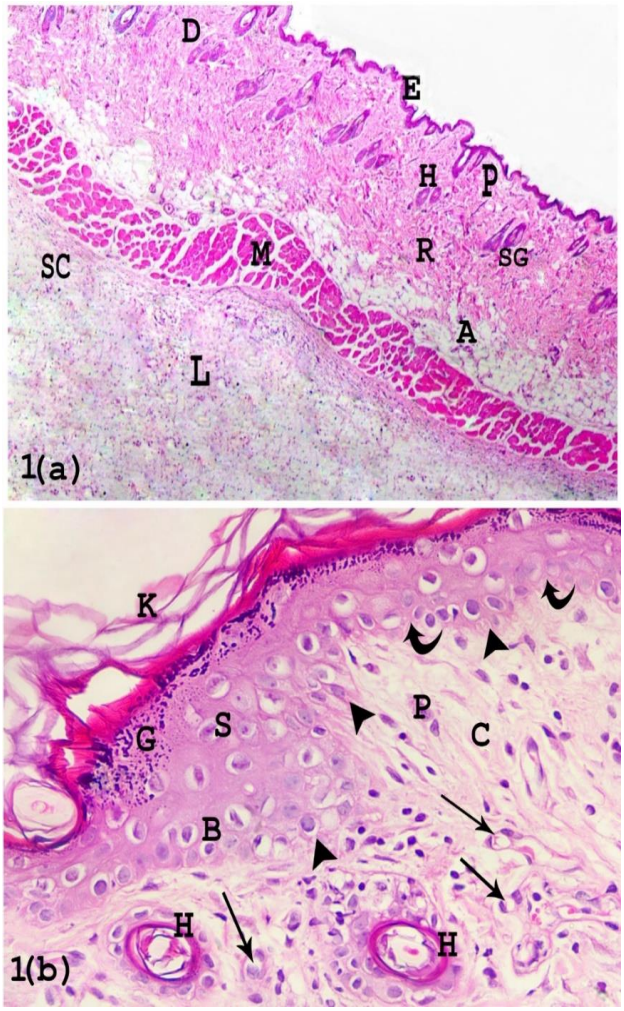

Fig. 1. A photomicrograph of control adult GpI shows, (a) the epidermis (E) and the dermis (D). The dermis consists of an outer papillary (P) and an inner reticular layers (R) containing hair follicles (H) associated with sebaceous glands (SG). The subcutaneous tissue (SC) consists of an outer layer of adipose tissue (A), a deep layer of loose connective tissue (L), and an interspersed band of striated muscle fibers (M) (H&E x 40). (b) The epidermis consists of stratum basale (B), spinosum (S), granulosum (G), corneum, and the outermost keratin lamellae (K). The rete ridges (arrow heads) interdigitate the dermal papillae at the epidermal-dermal junction (curved arrows). The superficial papillary layer (P) contains collagen fibers (C), blood capillaries (thin arrows), and hair follicles (H). (H&E x 400).

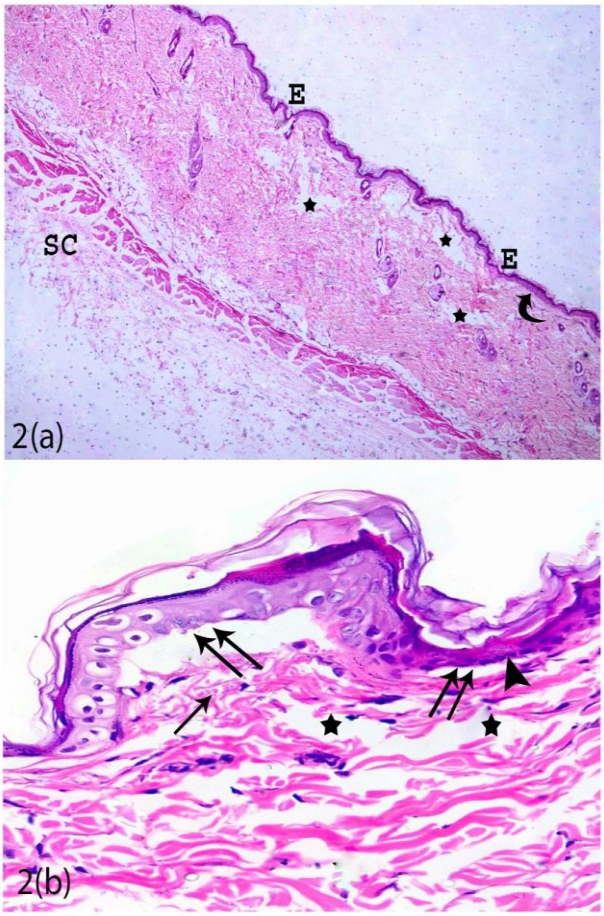

Fig.2. A photomicrograph of control aged GpII shows, (a) apparently focal regions of thin epidermis (E), flattening of epidermal-dermal junction (curved arrow) and the dermis displays empty areas (stars). Notice the relatively decreased thickness of subcutaneous tissue (SC) (H&E, x 40). (b) The epidermis shows focal separations from the underlying dermis (double arrows). A focal area of atypical keratinocytes displays homogenous acidophilic cytoplasm and darkly stained flattened nuclei (arrowhead). The papillary dermis exhibits some focal empty spaces (stars), and the collagen fibers appear disorganized, tangled, fragmented, and widely spaced (thin arrow) (H&E, x 400).

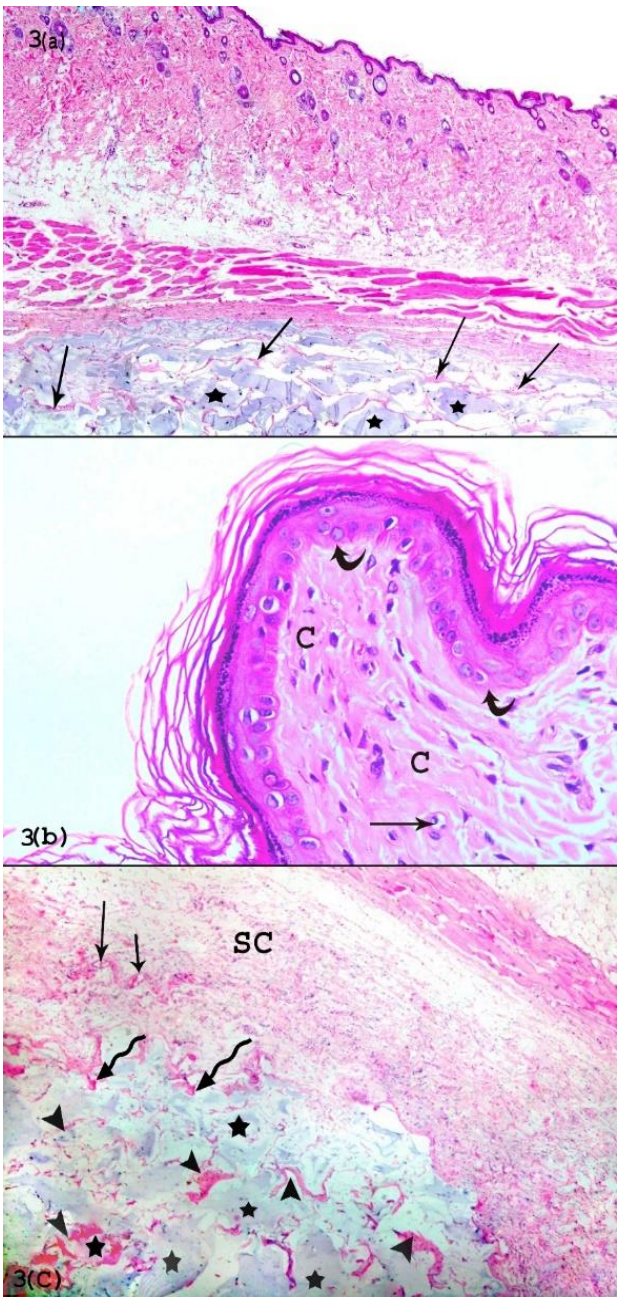

Fig. 3. A photomicrograph of HA-injected GpIII shows, (a) absence of empty spaces in the whole dermis. The subcutaneous tissue is seen well integrated with the basophilic, homogenous, and evenly distributed HA (stars), containing acidophilic collagen fibers (thin arrows) (H&E, x 40). (b) The apparently normal epidermis shows the known four layers with a well demarcated undulated epidermal-dermal junction (curved arrows). The papillary dermis displays well-organized collagen fibers (C), and blood vessels (thin arrow) (H&E, x 400). (c) At the periphery of the filling material, the subcutaneous tissue (SC) displays disseminated, integrated numerous collagen fibers (wavy arrows) and forms islands of dense connective tissue (arrowheads) in between HA filler (stars). Notice the presence of blood vessels (thin arrows) in the loose areolar layer of the subcutaneous tissue (H&E, x 400).

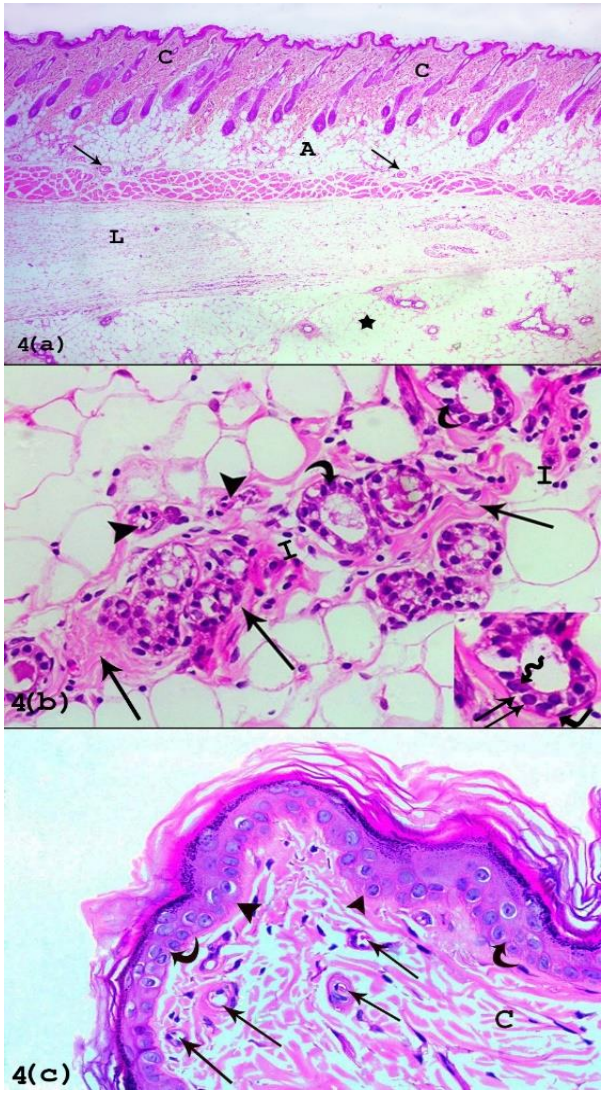

Fig. 4: A photomicrograph of nanofat-injected Gp IV shows (a) nearly normal epidermis and dermis that expresses well-organized, closely packed collagen fibres (C). The subcutaneous tissue exhibits a relative increase in the thickness of adipose tissue (A) and loose connective tissue (L). Notice increases in the number of blood vessels (thin arrows) in adipose layer of the subcutaneous tissue. The site of injection shows adipose tissue (star), compartmentalized by connective tissue septa (H&E, x40). (b) Numerous glandular acini of sweat glands (curved arrows), wavy acidophilic collagen fibres (thin arrows), numerous blood vessels (arrow heads), and inflammatory cells (I) are accommodated within the connective tissue septa. Dark (wavy arrow), clear (double arrows), and myoepithelial cells (right-angled arrow) line the sweat gland acinus (H&E, x400). (c) The epidermis is formed of the four usual layers and lies on a well-demarcated epidermal-dermal junction (curved arrows) with the presence of epidermal ridges (arrow heads). The papillary dermis contains collagen fibres (C) and numerous blood vessels (arrows) (H&E, x400).

Masson's trichrome-stained sections

Masson's trichrome staining of papillary dermis of GpI revealed fine, loosely arranged collagen fibers parallel to the basement membrane and deeper, dense, thick, wavy collagen bundles in the reticular dermis. The subcutaneous tissues displayed few collagen fibers (Fig. 5). The results of both subgroups IIa and IIb were the same. This group exhibited fragmentation of collagen fibers in the papillary dermis, disorganization, and clumps in the reticular layer of the dermis, along with focal loss in both layers of the dermis (Fig. 6). GpIII demonstrated an increase in closely packed collagen fibers and bundles in both the papillary and reticular layers of the dermis, in contrast to GpII. The newly formed collagen fibers were noticed in the subcutaneous tissue and within the area of injection by hyaluronic acid (Fig. 7). There was an obvious increase in the amount of collagen fibers in both papillary and reticular layers of the dermis of GpIV as compared to GpII. The area of nanofat injection displayed new collagen fibers that appeared beneath the muscle of the subcutaneous tissue and between adipose tissue (Fig. 8). Morphometrical analysis of the mean area percentage of collagen in Masson trichrome stained sections of GpII (20.502±4.209) revealed a significant decrease compared to GpI (36.469±6.514). A significant increase in GpIII (32.496±5.353) and GpIV (30.165±5.37) in comparison to GpI (36.469±6.514). A non-significant change was detected in GpIII and GpIV in comparison to GpI (Table 1, and Histogram 2).

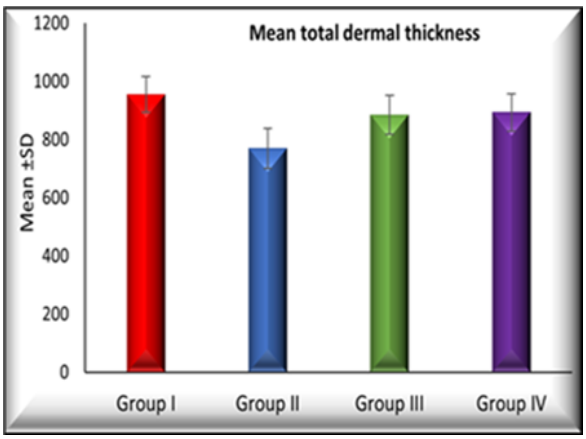

Histogram 1. Comparison between the studied groups regarding mean ± SD of total thickness of the dermis.

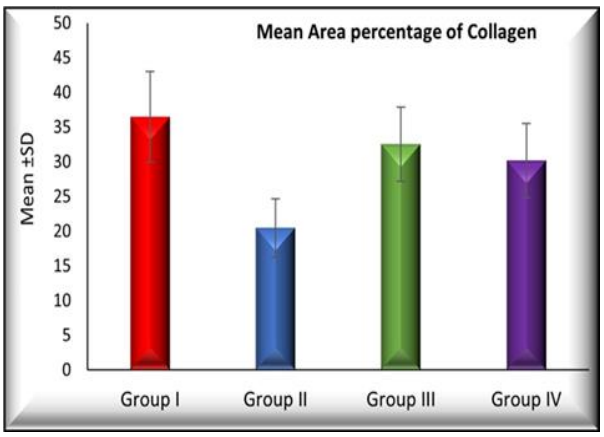

Histogram 2. Comparison between the studied groups regarding mean ± SD of mean area percentage of collagen.

Table 1. Morphometrical analysis of the different study groups

Parameters	GpI	GpII	GpIII	GpIV
Dermal thickness (um)	955.4±60.98	769.54±69.01[a]	885.0±66.09[b]	893.90±64.08[b]
Mean area percentage of collagen	36.46±6.51	20.50±4.20 [a]	32.49±5.35 [b]	30.16±5.37 [b]
Mean number of blood vessels	11.5±1.95	2.80±1.75[a]	6.60±3.20 [a,b]	10.20±3.61 [b,c]

Data is expressed as mean±SD, [a] indicates significance versus GpI, [b] indicates significance versus GpII, [c] indicates significance versus subgroup I

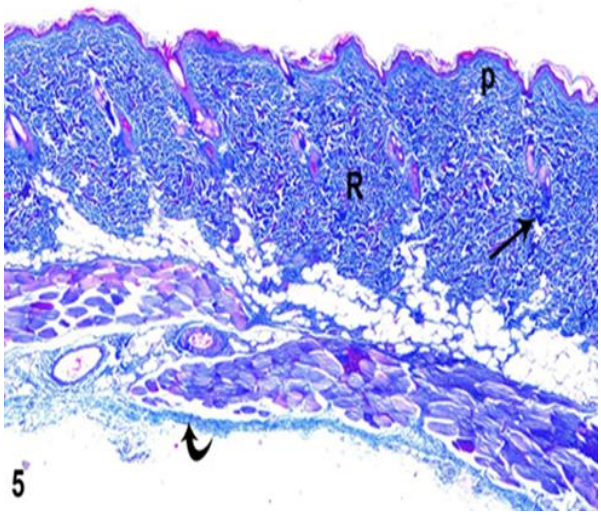

Fig. 5. A photomicrograph of GpI shows the fine interlaced collagen fibers in the papillary dermis (P) and the closely packed collagen bundles (thin arrows) appear in the reticular dermis (R). The subcutaneous tissue contains a few collagen fibers (curved arrow) (Masson's trichrome x 40).

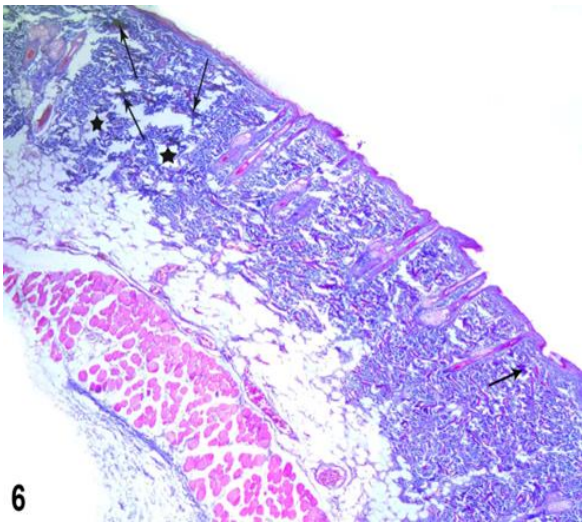

Fig. 6: A photomicrograph of GpII shows disorganized clumps of collagen fibers (thin arrows) with focal loss of collagen fibers in some areas (stars). Notice the decrease of collagen content in subcutaneous connective tissue (Masson's trichrome, x40).

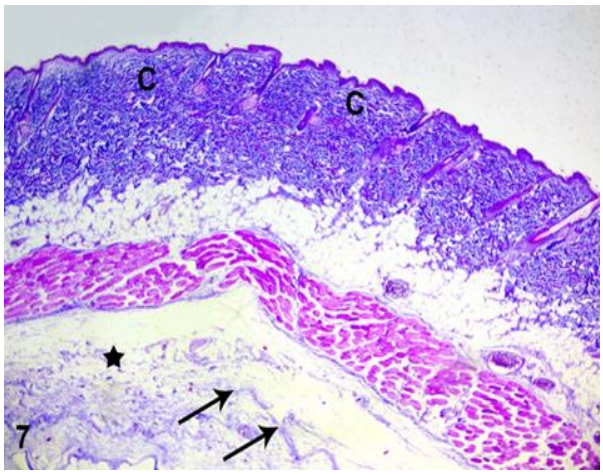

Fig. 7. A photomicrograph of GpIII shows well organized collagen fibers (C) in both layers of the dermis as well as marked increase in collagen fibers (thin arrows) in the subcutaneous tissue and within the area of injection (stars) (Masson's trichrome, x 40).

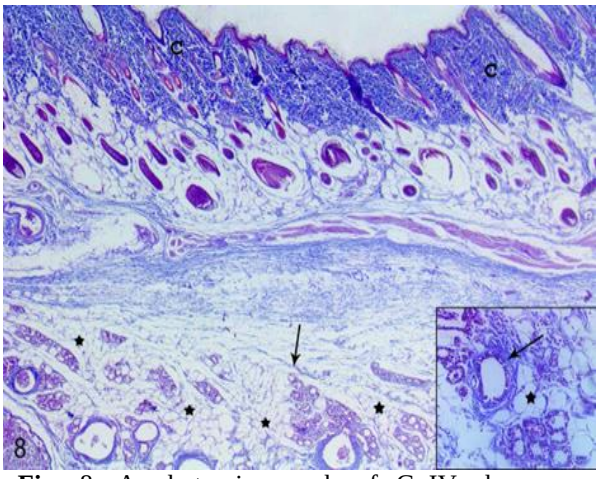

Fig. 8. A photomicrograph of GpIV shows an increase of collagen fibers (C) in the whole dermis. Notice the new collagen fibers (thin arrows) within the area of nanofat injection (stars) and in between the adipocytes in the subcutaneous tissue (Masson's trichrome, x 40; inset x 200).

Immunohistochemical staining results for VEGF

In GpI, immunohistochemical staining of VEGF revealed a positive brownish cytoplasmic reaction in the endothelium of the blood vessels and capillaries within both the papillary and reticular layers, as well as in the subcutaneous tissue (Fig. 9). Expression of the VEGF reaction also appeared in the keratinocytes of the epidermis, hair follicles, and sebaceous glands in all groups. GpII's dermis contained a few VEGF-positive blood vessels and capillaries (Fig. 10). The whole dermis of GpIII showed an increase in the number of blood vessels positive for VEGF compared with GpII (Fig. 11).

In GpIV, the entire dermis and subcutaneous tissue expressed a positive immune response for VEGF-positive blood vessels (Fig. 12). A positive reaction for VEGF was also observed in the cells in between the adipose tissue of subcutaneous tissue (Fig. 13).

The morphometric analysis of the mean number of VEGF-positive blood vessels in GpII (2.800±1.751) was significantly decreased compared to GpI (11.500±1.958), GpIII (6.600±3.204), and GpIV (10.200±3.615). However, VEGF immune reaction in GpIII was significantly decreased compared to GpI and GpIV and displayed an insignificant difference compared to GpI. Interestingly, GpIV showed a significant increase compared to GpIII. (Table 1, and Histogram 3).

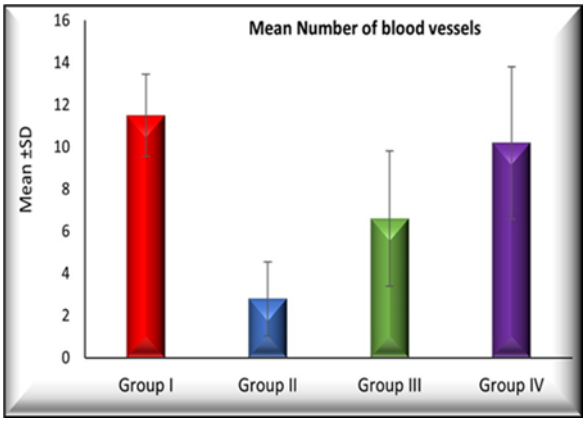

Histogram 3. Comparison between the studied groups regarding mean ± SD of number of blood vessels.

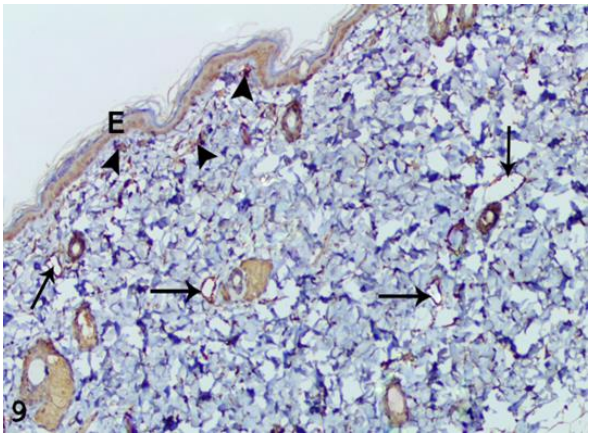

Fig. 9. A photomicrograph of GpI shows brownish positive immune reactions for VEGF in the endothelium of many blood vessels of the papillary layer (arrowheads), and reticular layer (thin arrows) (VEGF x 200).

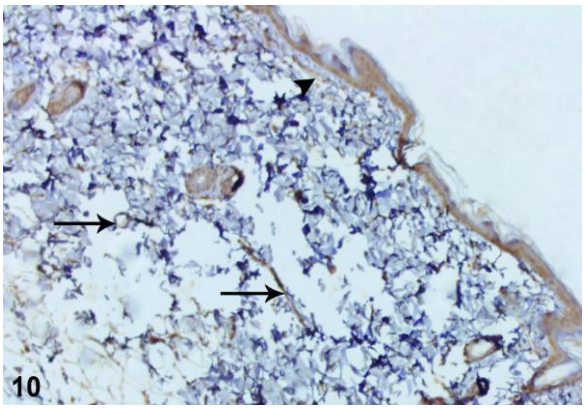

Fig. 10. A photomicrograph of GpII shows positive immune reactions for VEGF in the endothelium of the few blood vessels of papillary layer (arrowheads), as well as reticular layer (thin arrows) of the dermis (VEGF x 200).

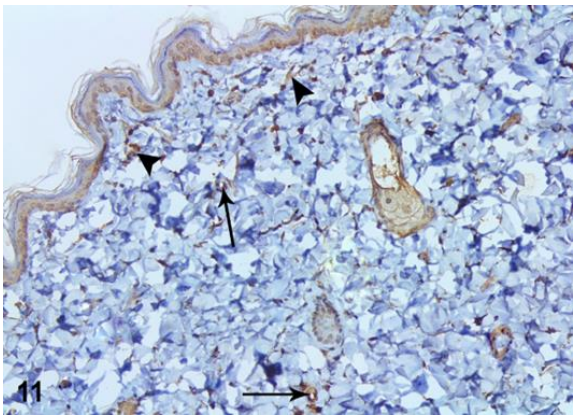

Fig. 11. A photomicrograph of GpIII shows an increased number of the positively stained VEGF blood vessels of papillary layer (arrowheads) and in the reticular layer (thin arrows) of the dermis (VEGF x 200).

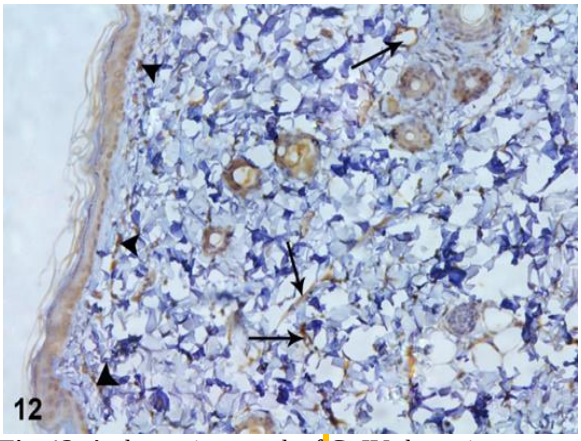

Fig. 12. A photomicrograph of GpIV shows increases in the positive immune reaction for VEGF in the endothelium of many blood vessels of papillary layer **(**arrowheads) and the reticular layer (thin arrows) of the dermis (VEGF x 200).

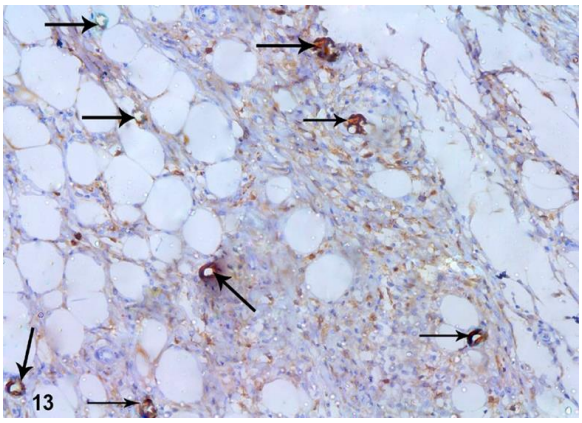

Fig.13. A photomicrograph of GpIV shows an intense brownish positive immune reaction for VEGF in the endothelium of many blood vessels (thin arrows) in the subcutaneous tissue and moderately positive reaction of the cells in between the adipose tissue (VEGF x 400).

Electron microscopic results

Electron microscopic examination of GpI showed that the epidermis was formed of stratified keratinocytes organised into four layers. The stratum basale consisted of low columnar cells that rest on and bind to a thin, continuous basement membrane and featured multiple hemidesmosomes. Adjacent to basale cells were stratum spinosum cells and granulosum cells containing electron dense keratohyalin granules. The outermost layer was stratum corneum, composed of keratin lamellae (Fig. 14). The papillary dermis revealed fine, interlacing collagen fibers (Fig. 14), while the reticular dermis showed thick, regularly

arranged, closely packed collagen bundles running in different directions. The bundles were consisted of parallel fibers with the characteristic cross striations (Fig. 15), in between there were large parallel elastic fibers of moderate electron density (Fig. 16). Fibroblasts were spindle shaped with many cytoplasmic processes and displayed large, oval euchromatic nuclei, numerous rough endoplasmic reticulum (RER) and multiple mitochondria (Figs. 15 and 17). Electron microscopic picture of GpII showed some basale cells were lying on an ill-defined basement membrane with attenuated hemidesmosomes. Spinosum cells showed variability in size, wide intercellular spaces, and attenuated desmosomal junctions. The papillary dermis exhibited split, tangled, fragmented collagen fibers, along with widely spaced, relatively small, and disorganized bundles (Figs. 18 and 19).

The reticular dermis revealed separated, deformed, relatively small collagen bundles made of randomly arranged and dispersed fibers, accompanied by fragmented elastic fibers (Figs. 20 and 21). Some fibroblasts appeared smaller in size with electron dense cytoplasm and few, short cytoplasmic processes (Fig. 19). Furthermore, some fibroblasts seemed shrunken with withdrawn cytoplasmic processes and contained cytoplasmic vacuoles, secondary lysosomes, and membrane blebs. The nuclei were indented with peripheralization of their chromatin. Many apoptotic bodies were resided in between the spaced collagen bundles (Fig. 20). The ultrathin sections of GpIII showed that the epidermis closely resembled the adult group. The basale cells were resting on a thin, continuous basement membrane with multiple hemidesmosomes, and the keratinocytes were interconnected by desmosomal junctions with normal intercellular spaces. The papillary dermis revealed fine, interlacing collagen fibers and small bundles (Fig. 22). In reticular dermis, the bundles seemed somewhat packed and relatively thicker than those in group II and contained highly ordered, uniformly distributed collagen fibers. However, a few localized bundles exhibited separated irregular fibers (Fig. 23). Large electron dense elastic fibers were observed in-between the packed collagen bundles (Fig. 24). The fibroblasts were elongated with euchromatic nuclei and prominent nucleoli, numerous slightly dilated RER, mitochondria, and a few cytoplasmic vacuoles contained electron dense material (Fig. 25). The examination of GpIV showed that basale cells rest on a thin basement membrane, and spinosum cells interdigitated with each other by junctional desmosomes. The papillary dermis revealed a relatively coarse collagen fibers as well as small, tightly packed collagen bundles (Fig. 26). Regarding the reticular dermis, the bundles were closely packed and showed obvious increase in the diameter compared to GpII and GpIII. The fibers were thick, parallel, and regularly arranged with the characteristic cross striations in their longitudinal sections (Fig. 27). Immature elastic fibers were bounded by thick collagen bundles (Fig. 28). Fibroblasts exhibited activity features with many cytoplasmic processes, numerous dilated RER, mitochondria, and large, oval, euchromatic nuclei. However, some multiple cytoplasmic vacuoles were also seen (Figs 27 and 29).

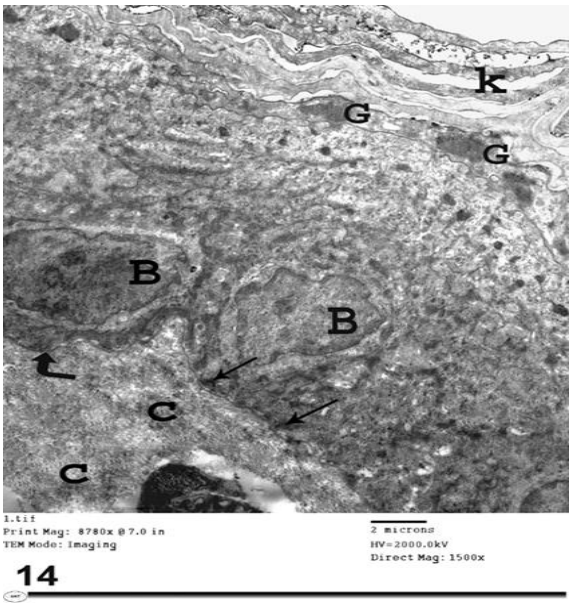

Fig. 14. An electron micrograph of GpI depicts two basale cells (B) bind to a thin continuous basement membrane (angled-right arrow) with multiple hemidesmosomes (thin arrows). The granulosum cells (G) contain electron dense keratohyaline granules, and the stratum corneum comprises keratin lamellae (K). The papillary dermis contains fine interlacing collagen fibers (C) (Mag x 8780).

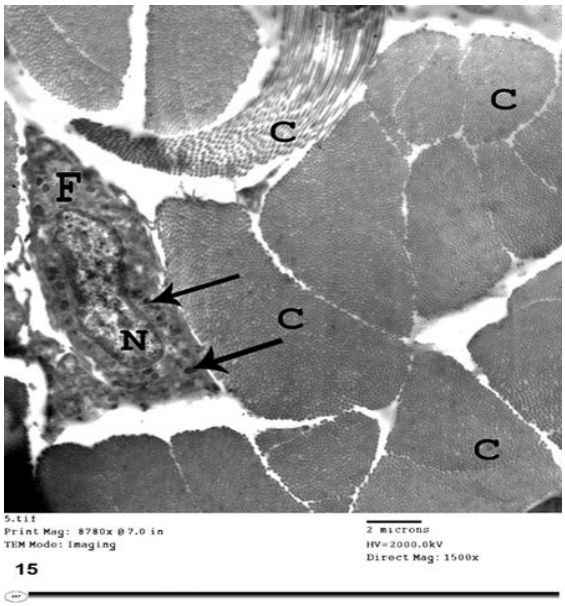

Fig .15. An electron micrograph of the reticular dermis of GpI shows a fibroblast (F) with euchromatic, oval, nucleus (N) and multiple mitochondria (thin arrows). Collagen bundles (C) appeared thick, well organized and closely packed running in different directions. They display uniformly distributed collagen fibers (Mag x 8780).

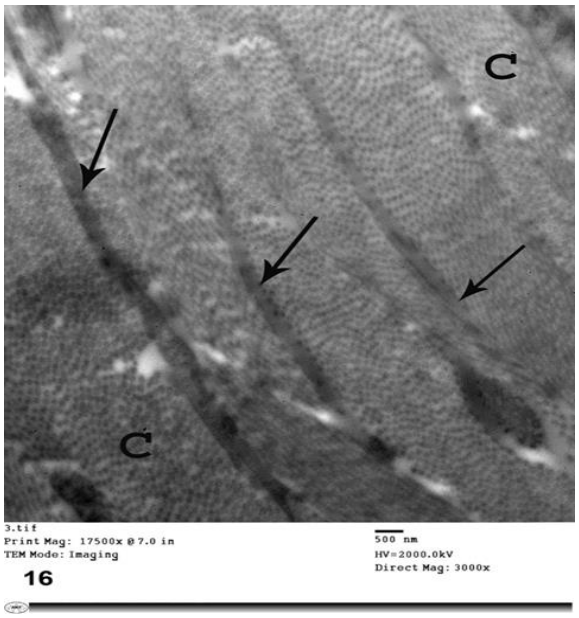

Fig.16. An electron micrograph of the reticular dermis of GpI shows thick tightly packed collagen bundles (C) bounded by large parallel elastic fibers (thin arrows) with moderate electron density (Mag x 17500).

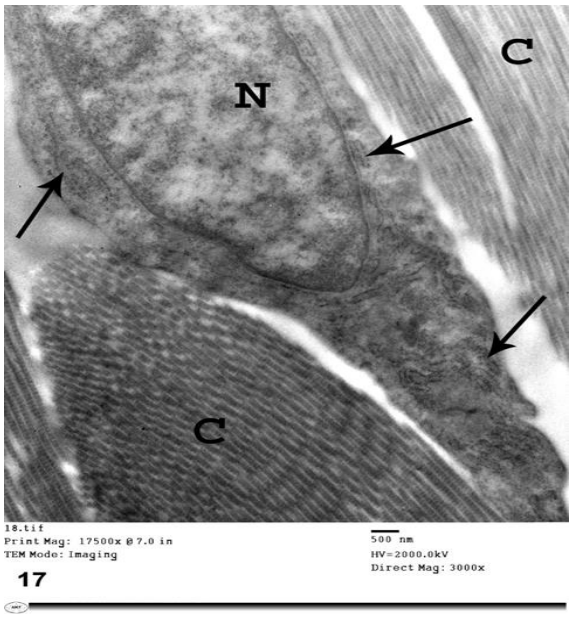

Fig. 17. An electron micrograph of the reticular dermis of GpI shows a spindle-shaped fibroblast with an oval, euchromatic nucleus (N) and numerous RER (thin arrows). Collagen bundles (C) appear tightly packed, thick, and composed of regularly arranged parallel, thick fibers with the characteristic cross striations in their longitudinal sections. (Mag x 17500).

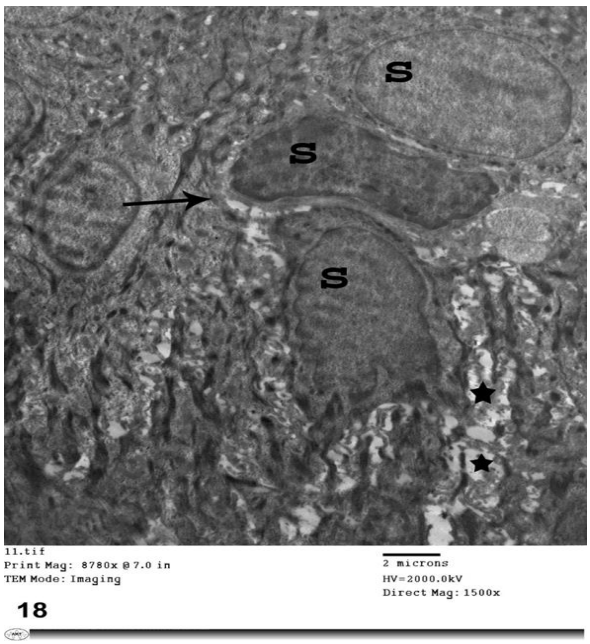

Fig.18. An electron micrograph of control aged GpII shows wide intercellular spaces (stars) in between some spinosum cells (S) with attenuation of the desmosomal junctions (thin arrows) (Mag x 8780).

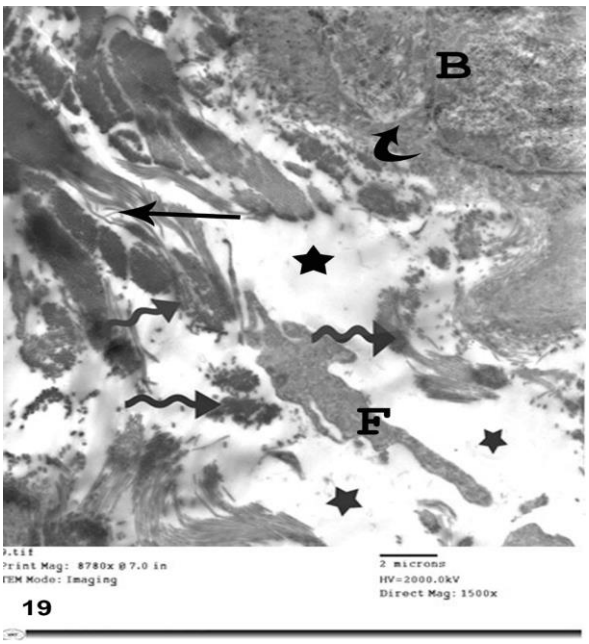

Fig.19. An electron micrograph of GpII shows a basale cell (B) is lying on an ill-defined basement membrane with attenuated hemidesmosomes (curved arrow). The papillary dermis reveals split (thin arrow) and fragmented (wavy arrows) collagen fibers, with empty spaces (stars) between them. A small fibroblast (F) with short cytoplasmic processes and electron dense cytoplasm was also noticeable. Notice inconspicuous cytoplasmic organelles (Mag x 8780)

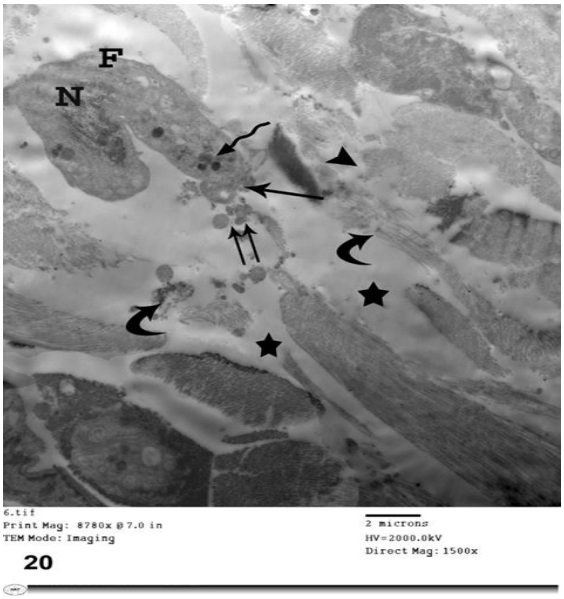

Fig. 20. An electron micrograph of the reticular dermis of GpII shows a shrunken fibroblast (F) with an indented condensed nucleus (N) with chromatin margination and displays withdrawn cytoplasmic processes, cell membrane blebbing (arrow), vacuolated cytoplasm, and secondary lysosomes (wavy arrows). Notice multiple apoptotic bodies (double arrows). Widely spaced (stars), disorganized deformed collagen bundles (arrowhead) are seen formed of disordered, dispersed and fragmented fibers (curved arrows) (Mag x 8780).

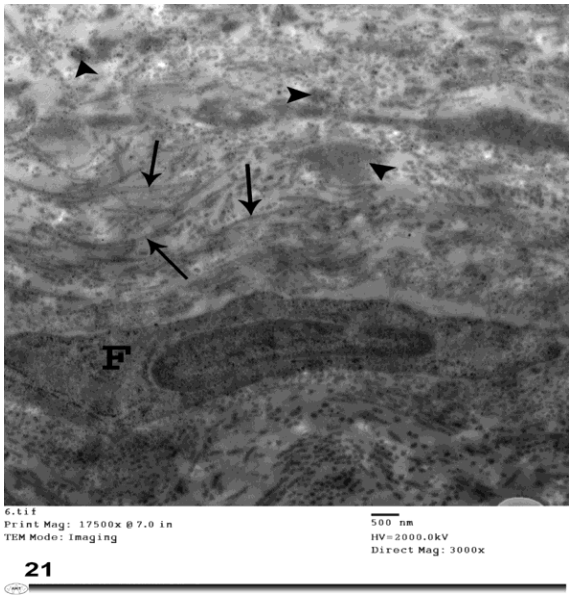

Fig.21. An electron micrograph of the reticular dermis of GpII shows a fibroblast (F) with disrupted nuclear membrane and peripheral chromatin margination surrounded by disintegrated, thin, fragmented collagen (thin arrows) and elastic fibers (arrow heads) (Mag x 17500).

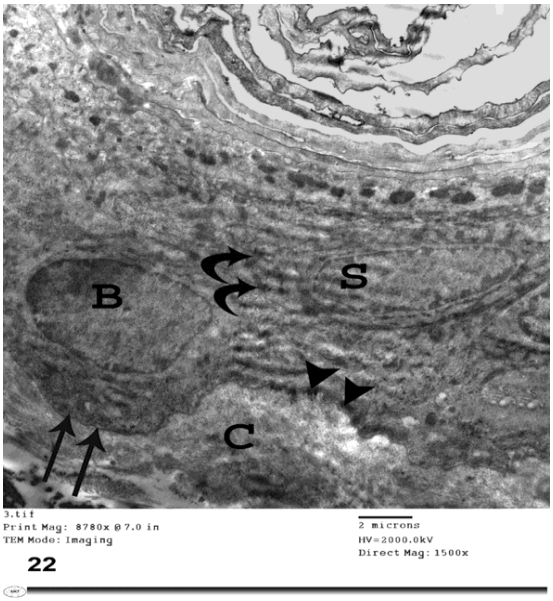

Fig. 22. An electron micrograph of GpIII shows a basale cell (B) lies on and binds to a well-defined basement membrane (thin arrows) with multiple hemidesmosomes (arrowheads). A spinosum cell (S) bridges the normal intercellular spaces with numerous desmosomes (curved arrows). Notice the fine interlacing collagen (C) fibers in the papillary dermis (Mag x 8780).

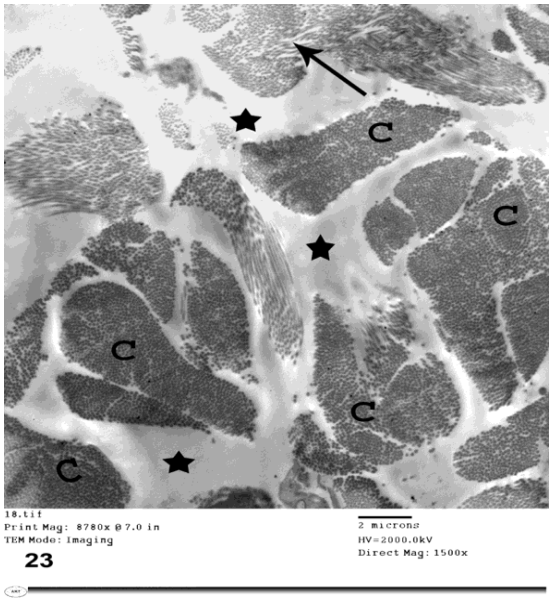

Fig. 23. An electron micrograph of the reticular dermis of GpIII shows slightly packed (stars) and relatively thick collagen bundles (C) formed of regularly arranged fibers. Notice the bundle containing separated irregular fibers (thin arrow) (Mag x 8780).

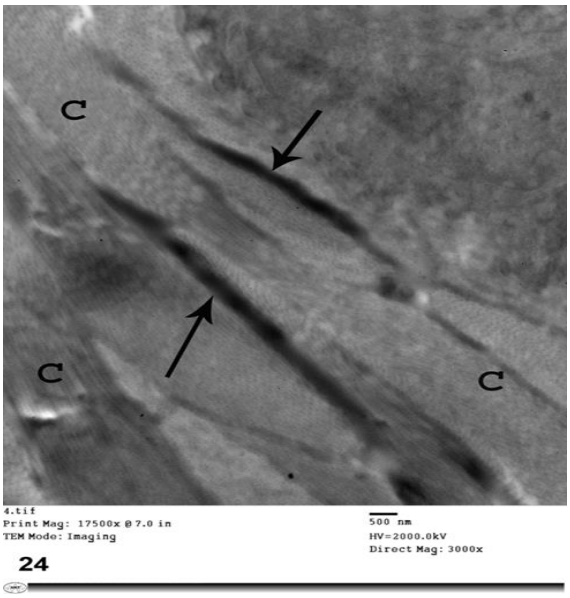

Fig. 24. An electron micrograph of the reticular dermis of GpIII shows large electron dense elastic fibers (thin arrows) in-between the packed collagen bundles (C) (Mag x 17500).

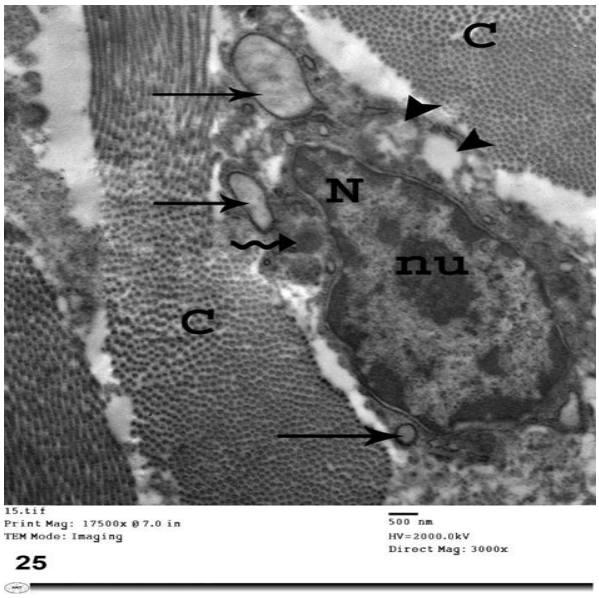

Fig. 25. An electron micrograph of the reticular dermis of GpIII shows a part of fibroblast containing a large, oval, euchromatic nucleus (N) with a prominent nucleolus (nu), numerous dilated RER (thin arrows), mitochondria (wavy arrow), and few vacuoles (arrow heads). The thick, compact collagen bundles (C) are composed of highly ordered and uniformly distributed fibers (Mag x 17500).

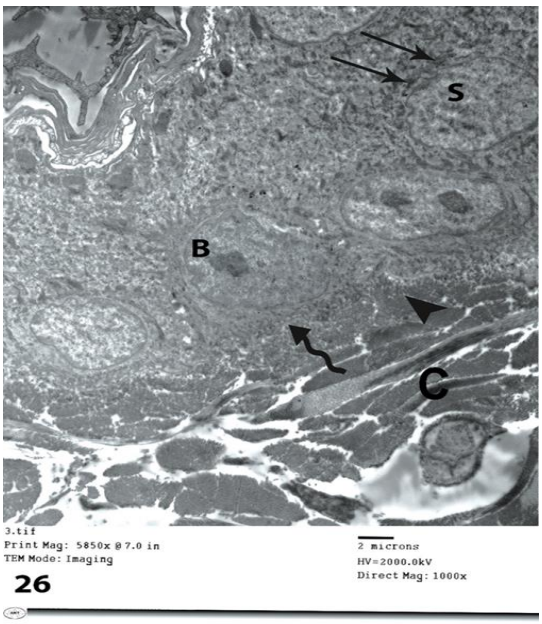

Fig. 26. An electron micrograph of GpIV shows basale cell (B) rest on a thin basement membrane (wavy arrow) and a stratum spinosum cell (S) interconnected by desmosomes (thin arrows). The papillary dermis contains coarse collagen fibers (arrowhead) and small, packed collagen bundles (C) (Mag x 5850).

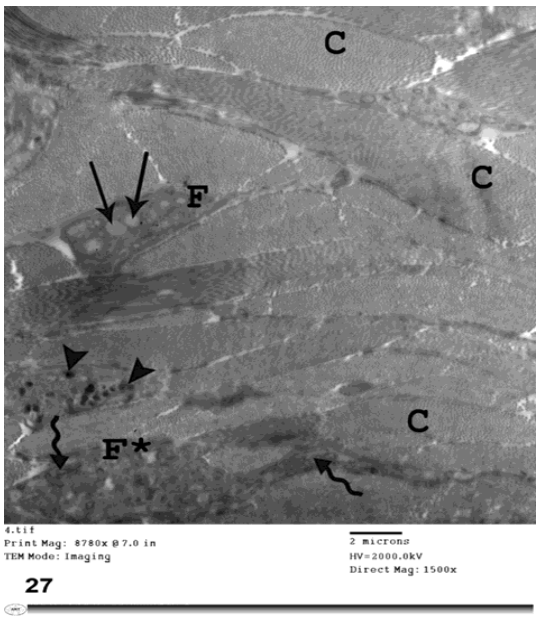

Fig. 27. An electron micrograph of the reticular dermis of GpIV appears crowded with thick, tightly packed collagen bundles (C). Parts of fibroblasts (F) have mitochondria (arrow heads) and cytoplasmic vacuoles (thin arrows). Notice the active, plumped fibroblast (F*) with cytoplasmic processes and numerous dilated RER (wavy arrows) (Mag x 8780).

Fig. 28. An electron micrograph of the reticular dermis of GpIV shows immature elastic fibers composed of amorphous substances, fibrillin (thin arrow) bounded by thick tightly packed collagen bundles (C) (Mag x 17500).

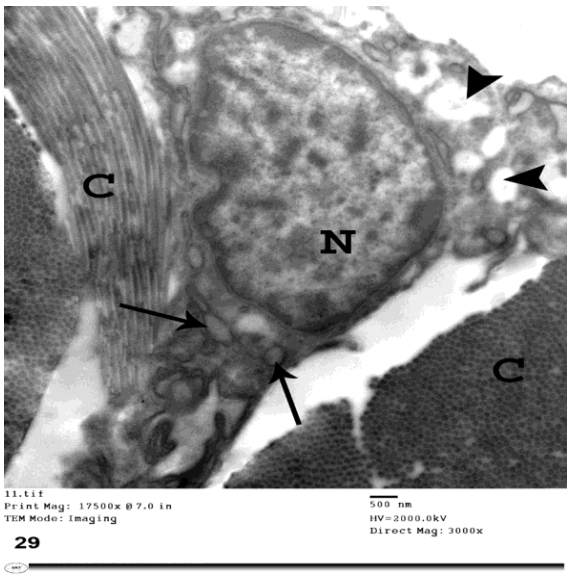

Fig. 29. An electron micrograph of GpIV shows a fibroblast with an euchromatic nucleus (N), cytoplasmic processes, dilated RER (thin arrows), and some cytoplasmic vacuoles (arrowheads) in between the thick, compact collagen bundles (C) (Mag x 17500).

Discussion

Skin ageing is an inevitable biological process that is caused by intrinsic and extrinsic factors (Kerns and Chien, 2019). HA and nanofat are dermal fillers that are commonly used nowadays to create volume or reverse any soft tissue loss (Hernandez et al., 2023; Li et al., 2023). The present work was designed to compare the anti-ageing effect of HA versus nanofat .injections on the aged skin of female albino rats. Although female skin is thinner than that of males, it has receptors for estrogen, androgen, luteinizing hormone, and follicular stimulating hormones. Estrogen increases epidermal thickness and enhances skin moisture by boosting vascularization, increasing glycosaminoglycans, such as HA, and increasing collagen production in the dermis. Despite estrogen not being directly involved in the regulation of collagen synthesis, it can play a role in the organization and stability of collagen fibrils (Misiakiewicz-Has et al., 2020).

In the current work, the light (LM) and electron microscope (EM) examinations of the epidermis of GpIII that was injected with HA appeared nearly similar to control adult GpI, with restoration of the epidermal-dermal junction, normal intercellular spaces, and prominent desmosomes. This was in agreement with Chen et al. (2023), who noticed that the low molecular weight HA complex caused an enhanced tightness between the basal keratinocytes and the basement membrane, resulting in reconstruction of the full thickness of the epidermis. HA also enhanced the expression of epidermal-dermal junction proteins such as laminin-332 and fibrillin-1. As regards the LM examination of the dermis of the same group, the collagen bundles were well organized and showed a significant increase in the dermal thickness and in the mean area percentage of Masson trichrome-stained fibers in comparison to GpII and a non-significant change compared to GpI. By EM, the collagen bundles appeared thicker and slightly more packed than those in GpII, accommodating large, electron dense elastic fibers and elongated fibroblasts with dilated RER and euchromatic nuclei in between. The increased dermal thickness in GpIII agreed with Bukhari et al. (2018) and Sun et al. (2023), who observed an increase in the mature elastic and the newly synthesized collagen fibers at the site of filler injection. Furthermore, HA filler promotes fibroblast proliferation and viability and increases type I collagen without causing apparent inflammation (Cabral, et al., 2020). Fan et al. (2019) and Chen et al. (2023) explained that the low molecular weight HA can simultaneously suppress MMP-1 and elastase expression with a subsequent decrease in collagen and elastic fragmentation. Abatangelo et al. (2020) stated that following the induction of HA to the damaged areas of skin, it flows into the fragmented fibers and creates a rigid scaffold that enhances mechanical tension and stimulates fibroblasts to produce new intact elastic and collagen fibers. Mochizuki et al. (2018) and Varì et al. (2022) indicate that after four weeks of HA filler injection, dermal fibroblasts were stimulated by mechanical stress, resulting in the production of growth factors and tissue inhibitors of matrix metalloproteinases. This resulted in enhanced quality of the dermal and subcutaneous tissues. Moreover, it directly stimulates the surrounding fibroblasts by means of hyaluronan receptors such as CD44, expressed on their cell membrane, and cause their migration and proliferation, resulting in an increase in the extracellular matrix components (Antonio and Arroyo, 2021).

As regard VEGF expression in the dermis and subcutaneous tissue of GpIII, a significant increase in the blood vessel number compared to GpII was observed. It was found that the injection of HA-based biomaterials boosts angiogenesis essential for wound healing (Karam et al., 2023) and promotes endothelial cell proliferation and migration by targeting specific receptors such as CD44 for hyaluronan-mediated motility and toll-like receptor 4 (Queisser et al., 2021). Additionally, HA facilitates

angiogenesis of mesenchymal stem cells and endothelial colony-forming cells linked to the activation of the CD44/miR-139-5p pathway, hence enhancing severe limb ischemia (Luo et al., 2022). Hyaluronan can slightly increase the expression of angiogenic markers, including CD31 and Von Willebrand factor (Wu et al., 2022). In the current study, the subcutaneous tissue was increased in thickness and filled with the dispersed filler between the interlaced connective tissue fibers, indicating a successful integration. Braga et al., (2023) found that following HA injection, the host tissue experiences a foreign body reaction, where the monocytes migrate to the tissue and differentiate into macrophages. Macrophages and platelets secrete TGF-B, PDGF, promoting fibroblast migration, and endothelial cell chemotaxis. This is followed by a slow, gradual fibrous tissue synthesis that fixes the gel material to the host tissue and stabilizes it. This reaction was very expressive after one month and subsided after two months. Regarding nanofat-injected GpIV, the epidermal examination by light and electron microscopes appeared nearly similar to the control adult GpI with the appearance of epidermal ridges, eminent epidermal-dermal junction, normal intercellular spaces, and prominent junctional desmosomes. This was in line with Menkes et al. (2020), who attributed it to the pro-angiogenic growth factors in nanofat and the increased capillary density in the dermis. Nanofat grafting in wound healing enhanced healing duration and facilitated re-epithelialization by generating a para-keratinized, immature stratified epithelium. This was attributed to the substantial proliferative capacity of ADSCs and their capability to differentiate into mesodermal, ectodermal, and endodermal lineages. They can differentiate into keratinocytes and fibroblasts, in addition to secreting soluble mediators with angiogenic and anti-inflammatory properties (Elsherbeny et al., 2023).

Concerning the dermis of GpIV, there was a significant increase in the dermal thickness and the mean area percentage of Masson trichrome-stained collagen fibers compared to group II and a non-significant change compared to GpI and GpIII. LM and EM examination revealed thick, closely packed collagen bundles consisting of well-organized, thick fibers, housing in between immature elastic fibers and active fibroblasts containing numerous dilated RER and euchromatic nuclei. The regenerative effect of nanofat is attributed to the presence of SVF and ADSCs (Cicione et al., 2023). ADSCs differentiation results in significantly upregulated dermal fibroblasts that produce a large amount of type I collagen and smaller amounts of elastin protein with a subsequent secretion of greater amounts of matrix components that reconstruct and rehabilitate the skin structure (Ding et al., 2022). Exosomes derived from ADSCs can be absorbed by fibroblasts, enhancing their ability to proliferate and migrate, promoting more deposition of fibrillin and collagen types I and III (Sanda et al., 2022). The activated fibroblasts release numerous microvesicles containing metalloproteinase-9 into the surrounding media. These microvesicles stimulate collagen remodeling by gradually transforming the collagen matrix from a laminar to a fibrillar type (Laghezza et al., 2016).GpIV revealed a significant increase in VEGF-positive blood vessel numbers in the dermis and subcutaneous tissue compared to groups II and III, and a non-significant change was observed compared to GpI. This came in accordance with Xu et al. (2018) who reported that the subcutaneous injection of nanofat increases dermal neovascularization in a photoaging skin model. These results were explained by Weinzierl et al. (2022) who reported that nanofat contains intact microvessel segments, which develop into well-organized vascular networks consisting of arterioles, capillaries, and venules. These networks develop interconnections with the microvasculature of the host tissue, resulting in a rapid onset of blood perfusion within the grafts. In addition, they progressively grow out of the grafts and improve the vascularization of the surrounding

transplantation site. Adipose-derived mesenchymal stem cells enhance endothelial cell proliferation and migration while reducing apoptosis, differentiate into endothelial vascular cells, and exhibit features of pericytes, resulting in the formation of capillary-like tubes as an early vascular network. This occurs through the release of VEGF, FGF-2, TGF-β, and insulin-like growth factor-1 (La Padula et al., 2023).

The subcutaneous tissue of GpIV, H&E and Masson trichrome-stained sections displayed increased thickness, and the area below the muscle was filled with areolar and adipose tissues. The injected area showed discrete cellular areas composed of collagen fibers, blood vessels, and eccrine sweat glands in between groups of many adipocytes. Gu et al. (2018) mentioned that the ADSCs in nanofat can regenerate sweat glands through the secretion of different growth factors. Also, they can be differentiated after co-culture in a Transwell system, and the epidermal growth factor can enhance differentiation efficiency. Besides, ADSCs may serve as a potential source of cells for sweat gland regeneration (Qiang et al., 2020). Furthermore, the ADSCs of nanofat can differentiate into fibroblasts and adipocytes (La Padula et al., 2023), and SVF contains pre-adipocytes and endothelial precursor cells (Cicione et al., 2023). Finally, it could be concluded that subcutaneous injection of both hyaluronic acid and nanofat significantly improved the signs of skin ageing by maintaining the epidermal-dermal junction, increasing the thickness of the dermis, activating fibroblasts, and promoting collagen and elastic synthesis. However, nanofat injection was superior to HA in neocollagenesis and neovascularization. Further researches are needed to study long-term expectations for each type and the different advantages that make each type preferable to the other.

5. Reference

Abatangelo G, Vindigni V, Avruscio G, Pandis L, Brun P, 2020. Hyaluronic Acid: Redefining Its Role. Cells. Jul 21;9(7):1743.

Allen J, Dodou, K, 2024. Current Knowledge and Regulatory Framework on the Use of Hyaluronic Acid for Aesthetic Injectable Skin Rejuvenation Treatments. Cosmetics, 11:54.

Antonio CR, Arroyo T L, 2021. The Importance of Interaction between Hyaluronic Acid and CD44 Receptor. Surgical and Cosmetic Dermatology. 13.

Aziz M, Gamal El Din E, Ahmed S, Ahmed Mekway, M, 2019. Histological Study on the Effect of Hyaluronic Acid Injection (Dermal Filler) on the Skin of the Adult and Aged Albino Rat. Egyptian Journal of Histology, 42(2): 245-261.

Bancroft and Layton, 2019. Chapter 10, the hematoxyline and Eosin in Bancroft, J.D.; Layton, C. and Suvarna SK. Bancroft's Theory and Practice of Histological Techniques. Eighth Edition, Elsevier, Oxford. P: 126-129.

Birch J, Gil J, 2020. Senescence and the SASP: Many Therapeutic Avenues. Genes and Development. 34: 1565–1576.

Braga CM, Rebouças C, Melo D N, Nunes A, Góes, Morais M, Leitão RF, 2023. Comparative Morphological Characterization of Skin after Subcutaneous Application of Hyaluronic Acid and Polycaprolactone in Rats: Establishment of an Experimental Model.

Bukhari S N A, Roswandi NL, Waqas M, Habib H, Hussain F, Khan S, Sohail M, Ramli NA, Thu H E, Hussain Z, 2018. Hyaluronic Acid, a Promising Skin Rejuvenating Biomedicine: A Review of Recent Updates and Pre-Clinical and Clinical Investigations on Cosmetic and Nutricosmetic Effects. International Journal of Biological Macromolecules. 120:1682–1695.

Cabral LRB, Teixeira LN, Gimenez RP, Demasi A. PD, de Brito Junior RB, de Araújo VC, Martinez EF, 2020. Effect of Hyaluronic Acid and Poly-L-Lactic Acid Dermal Fillers on Collagen Synthesis: An in vitro and in vivo Study. Clinical, Cosmetic and Investigational Dermatology. 13: 701–710.

Chen F, Guo X, Wu Y. Skin antiaging effects of a multiple mechanisms hyaluronan complex. Skin Res Technol. 2023 Jun;29(6): e13350.

Cicione C, Vadalà G, Di Giacomo G, Tilotta V, Ambrosio L, Russo F, Zampogna B, Cannata F, Papalia R, Denaro V, 2023. Micro-fragmented and Nanofat Adipose Tissue Derivatives: in Vitro Qualitative and Quantitative Analysis. Frontiers in Bioengineering and Biotechnology. 11: 911600.

Dawson-Saunders B, Trapp R, 2001. Basic and clinical biostatistics. 3rd ed. New York:Lange Medical Book/McGraw-Hill Medical Pub lishing Division. p 161–218.

Ding P, Lu E, Li G, Sun Y, Yang W, Zhao Z, 2022. Research Progress on Preparation, Mechanism, and Clinical Application of Nanofat, Journal of Burn Care and Research. 43:1140–1144.

Elsherbeny K, Elshahat A, Gad A, 2023. Effect of Autologous Nanofat Graft on the Healing of Donor Site of Split Thickness Graft. The Egyptian Journal of Plastic and Reconstructive Surgery. 47: 79-88.

Fan Y, Choi T H, Chung JH, Jeon YK, Kim S, 2019. Hyaluronic Acid-Cross-Linked Filler Stimulates Collagen Type 1 and Elastic Fibre Synthesis in Skin through the TGF-B/Smad jbjps.03.032 in A Nude Mouse Model. Journal of Plastic, Reconstructive and Aesthetic Surgery: JPRAS. 72: 1355–1362.

Gruber F, Kremslehner C, Eckhart L, Tschachler, 2020. Cell Ageing and Cellular Senescence in Skin Ageing - Recent Advances in Fibroblast and Keratinocyte Biology. Experimental Gerontology. 130: 110780.

Gu Z, Li Y, Li H, 2018. Use of Condensed Nanofat Combined with Fat Grafts to Treat Atrophic Scars. JAMA facial plastic surgery. 20: 128–135.

Guo J, Fang W, Wang F, 2023. Injectable fillers: current status, physicochemical properties, function mechanism, and perspectives. RSC advances. 13: 23841–23858.

Hernandez PM, Cotrin P, Valarelli FP, 2023 Evaluation of the Attractiveness of Lips with Different Volumes after Filling with Hyaluronic Acid. Sci Rep 13:4589.

Ho CY, Dreesen O, 2021. Faces of Cellular Senescence in Skin Ageing. Mechanisms of Ageing and Development. 198: 111525.

Jung-Bo H, Joo-Hyun K, Soyun K, So-Hyoun L, Kyung MS, Se EK, Seong SK, Chang-M.o J, 2015. Effects of PMMA and Cross-Linked Dextran Fillerfor Soft TissueAugmentation in Rats. International Journal of Molecular Sciences. 16: 28523–28533.

Karam J, Singer BJ, Miwa H, Chen LH, Maran K, Hasani M, Garza S, Onyekwere B, Yeh H C, Li S, Carlo DD, Seidlits SK, 2023. Molecular Weight of Hyaluronic Acid Cross-linked into Biomaterial Scaffolds Affects Angiogenic Potential. Acta Biomaterialia. 169: 228–242.

Kerns ML, Chien AL, 2019. Ageing Skin. Sewon Kang, Masayuki A, editors. Fitzpatrick's Dermatology. Ninth Edition. New York: McGraw-Hill Education. 2: 1779-9.

Krutmann J, Schikowski T, Morita A, Berneburg M, 2021, Environmentally Induced (Extrinsic) Skin Ageing: Exposomal Factors and Underlying Mechanisms. The Journal of Investigative Dermatology. 141:1096–1103.

Kuo J, 2016. Processing Biological Tissues for Ultrastructural Study in Electron Microscopy: Methods and Protocols. Third Edition, Humana Press Inc. Totowa, New Jersey. P.19.

Kushawaha S, Malpani A, Aswar UM, Bodhankar SL, Malpani A, Shivakumar S, 2011. Effect of Different Anesthetic Agents on Cardiovascular Parameters in Male Wistar Rats. Research Journal of Pharmaceutical, Biological and Chemical Sciences. 2:685-690.

La Padula S, Ponzo M, Lombardi M, Iazzetta V, Errico C, Polverino G, Russo F, D'Andrea L, Hersant B, Meningaud JP, Salzano G, Pensato R, 2023. Nanofat in Plastic Reconstructive, Regenerative, and Aesthetic Surgery: A Review of Advancements in Face-Focused Applications. Journal of Clinical Medicine.12(13): 4351.

Laghezza MV, Taddei, A R, Gambellini G, Giorgi F, Fausto AM, 2016. Microvesicles Shed from Fibroblasts Act as Metalloproteinase Carriers in a 3-D Ccollagen Matrix. Journal of Circulating Biomarkers. 5:1849454416663660.

Li X, Chiang CF, Lin YH, Chen TM, Wang CH, Tzeng YS, Cui HY, 2023. Safety and Efficacy of Hyaluronic Acid Injectable Filler in the Treatment of Nasolabial Fold Wrinkle: a Randomized, Double-Blind, Self-Controlled Clinical Trial, Journal of Dermatological Treatment. 34:1.

Liang Y, Su W, Wang F, 2023. Skin Ageing: A Progressive, Multi-Factorial Condition Demanding an Integrated, Multilayer-Targeted Remedy. Clinical, cosmetic and investigational dermatology. 16: 1215–1229.

Luo Y, Liang F, Wan X, Liu S, Fu L, Mo J, Meng X, Mo Z, 2022. Hyaluronic Acid Facilitates Angiogenesis of Endothelial Colony Forming Cell Combining with Mesenchymal Stem Cell via CD44/ MicroRNA-139-5p Pathway. Frontiers in Bioengineering and Biotechnology. 10: 794037.

Lynch B, Pageon H, Blay H, 2022. A Mechanistic View on the Ageing Human Skin through Ex Vivo Layer-By-Layer Analysis of Mechanics and Microstructure of Facial and Mammary Dermis. Sci Rep. 12: 849.

Mamizadeh M, Tahmasebi Ghorabi S, Mansourinia Z, Shadfar F, Karimi Rouzbahani A, 2024. Comparison the Effect of Conventional and Nanofat Injection Methods on Nasolabial Fold Lipofilling: A Case- Control Study. World journal of plastic surgery. 13: 24–31.

Menkes S, Luca M, Soldati G, Polla L, 2020. Subcutaneous Injections of Nanofat Adipose-derived Stem Cell Grafting in Facial Rejuvenation. Plastic and reconstructive surgery. Global open. 8(1): e2550.

Misiakiewicz-Has K, Zawiślak A, Pilutin A, Kolasa-Wołosiuk A, Szumilas P, Duchnik E, Wiszniewska B, 2020. Morphological and Functional Changes in Skin of Adult Male Rats Chronically Treated with Letrozole, a Nonsteroidal Inhibitor of Cytochrome P450 Aromatase. Acta Histochem Cytochem. 2020. 53(5):99-111.

Mochizuki MAN, Gonda K, Hirabayashi S, Komuro Y, 2018. Evaluation of the in Vivo Kinetics and Biostimulatory Effects of Subcutaneously Injected Hyaluronic Acid Filler; Plast Reconstr Surg; 142 (1):112-121.

Nguyen T, 2022. Immunohistochemistry: A Technical Guide to Current Practices. by TJ Books, Padstow Cornwall, Cambridge University Press. P 21.

Pilkington S M, Bulfone-Paus S, Griffiths C. E. M. and Watson, R E B, 2021): Inflammaging and the Skin. The Journal of Investigative Dermatology. 141:1087–1095.

Qiang S, Wang X, Zhang C, Liu Yi X, Zhi-Bo Li, Li F, Zhou Y, 2020. Conversion of Adipose-Derived Stem Cells into Sweat Gland-Like Cells: An in Vitro Phenotypic Study. International Journal of Dermatology and Venereology. Publish Ahead of Print. 1. 10.1097/JD9.0000000000000081.

Queisser KA, Mellema RA, Petrey AC, 2021, Hyaluronan and Its Receptors as Regulatory Molecules of the Endothelial Interface. Journal of Histochemistry and Cytochemistry.69(1):25-34.

Sanada A, Yamada T, Hasegawa S, Ishii Y, Haseb Y, Iwata Y, Arima M, Sugiura K, Akamatsu H, 2022. Enhanced Type I Collagen Synthesis in Fibroblasts by Dermal Stem /Progenitor Cell-Derived Exosomes. Biological and Pharmaceutical Bulletin. 45 (7): 872–880.

Sharma S, Muthu S, Jeyaraman M, Ranjan R, Jha S K, 2021. Translational products of adipose tissue-derived mesenchymal stem cells: Bench to bedside applications. World journal of stem cells.13(10): 1360–1381.

ShinJ W, Kwon SH, Choi JY, Na JI, Huh CH, Choi HR, Park KC, 2019): Molecular Mechanisms of Dermal Ageing and Anti-Ageing Approaches. International Journal of Molecular Sciences. 20(9): 2126.

Simonacci F, Bertozzi N, Grieco MP, Raposio E, 2019. From Liposuction to Adipose-Derived Stem Cells: Indications and Technique. Acta Biomed. Atenei Parmensis, 90(2):197-208.

Sun L, Sun X, Ruan W, 2023. Mechanism of Remodeling and Local Effects in Vivo of A new injectable cosmetic filler. Sci Rep 13: 9599.

Tonnard P, Verpaele A, Peeters G, Hamdi M, Cornelissen M, Declercq H, 2013. Nanofat Grafting: Basic Research and Clinical Applications. Plastic and Reconstructive Surgery. 132(4): 1017–1026.

Varì S, Minoretti P, Emanuele E, 2022. Human Dermal Fibroblast Response to Hyaluronic Acid-Based Injectable Dermal Fillers: An in vitro study. Advances in Dermatology and Allergology/Postępy Dermatologii i Alergologii, 39 (6): pp.1088-1092.

Weinzierl A, Harder Y, Schmauss D, Menger M, Laschke M, 2022. Boosting Tissue Vascularization: Nanofat as a Potential Source of Functional Microvessel Segments. Frontiers in Bioengineering and Biotechnology. 10: 820835.

Wong QY, Chew FT, 2021. Defining Skin Ageing and Its Risk Factors: A Systematic Review and Meta-Analysis. Sci Rep 11: 22075.

Wu GT, Kam J, Bloom JD, 2022. Hyaluronic Acid Basics and Rheology. Facial Plastic Surgery Clinics of North America. 30: 301–308.

Xu P, Yu Q, Huang H, Zhang WJ, Li W, 2018. Nanofat Increases Dermis Thickness and Neovascularization in Photoaged Nude Mouse Skin. Aesthetic plastic surgery. 42: 343–351.